TWENTY FIRST EUROPEAN ROTORCRAFT FORUM

Paper No. I.2

COMBINED NUMERICAL AND EXPERIMENTAL INVESTIGATIONS OF BVI-NOISE GENERATION AND RADIATION FROM THE HART-TEST CAMPAIGN

K.Ehrenfried, W.Geissler, U.Seelhorst, H.Vollmers

DEUTSCHE FORSCHUNGSANSTALT FÜR LUFT- UND RAUMFAHRT,
GÖTTINGEN, GERMANY

August 30-September 1,1995
SAINT PETERSBURG, RUSSIA

Paper nr.: I.2

Combined Numerical and Experimental Investigations of BVI-Noise Generation and Radiation from the Hart-test Campaign.

K. Ehrenfried; W. Geissler; U. Seelhorst; H. Vollmers

TWENTY FIRST EUROPEAN ROTORCRAFT FORUM
August 30 - September 1, 1995 Saint-Petersburg, Russia

COMBINED NUMERICAL AND EXPERIMENTAL INVESTIGATIONS OF BVI-NOISE GENERATION AND RADIATION FROM THE HART-TEST CAMPAIGN

by
K.Ehrenfried*
W. Geissler*
U.Seelhorst*
H.Vollmers*
DLR Institute of Fluid Mechanics
Bunsenstr.10
37073 Göttingen
Germany

Abstract

3D-velocity fields have been measured on a 40% scaled BO-105 modelrotor by Laser-Doppler-Velocimetry (LDV) during the HART-test campaign in the open test section of the DNW. On both advancing and retreating sides of the rotor the flowfields inside and adjacent to specified tip-vortices prior to Blade Vortex Interaction (BVI) have been measured by DLR (advancing side) and ONERA (retreating side). From the measured velocity fields vortex specific quantities like core size, strength, location with respect to the interacting blade (miss-distance) have been derived and can be used as realistic inputs for numerical codes. In the present study 2D-model calculations at BVI have been carried out to study both near field flows during blade vortex interaction as well as farfield acoustic effects utilizing a Kirchhoff solution procedure. Calculated acoustic data are finally compared with sound pressures from microphones measured during the HART-test campaign.

1. Introduction.

For the investigation of Blade Vortex Interaction Noise (BVI) several test campaigns on a BO-105 model rotor have been carried out recently in the DNW open test section with its excellent anechoic properties. In addition to direct noise measurements by an array of microphones in the far field of the rotor detailed pressure time histories have first been measured with as much as 124 in-situ pressure transducers on one reference blade during the Helinoise Aeroacoustic Rotor Test [1]. The pressures have been measured by means of a complex measuring equipment of DLR [2]. From these preceding tests new insight into the complicated features of BVI noise generation and radiation could already be detected.

In addition Higher Harmonic Control (HHC-) effects were studied during the HART- test campaign [3],[4] to investigate also Low Noise (LN) and Low Vibration-(LV) conditions of the rotor. Up to now the reasons are not known why specific HHC parameter settings lead to a lower noise or lower vibration level. A much more detailed knowledge of the flow structure of the tip-vortex system just before and during interaction with the rotor blade is necessary.

One major objective of the HART-test campaign was therefore to include in addition to acoustic- and pressure-measurements also flowfield measurements by LDV to be carried out in regions on both advancing and retreating sides of the rotor disc prior to blade vortex interaction. To limit the amount of measuring time, the LDV-measurements were jointly done by LDV set-ups of both DLR (advancing side) and ONERA (retreating side).

The present paper is concerned with some selected data obtained by the DLR 3D-LDV test set-up [5] on the ***advancing*** side of the rotor. For this purpose a new LDV test rig has been developed by DLR which is able to realize a measuring distance of more than 5m and thus can be operated in the open test section of the DNW. The objectives of the LDV tests were to

- measure the velocity distributions inside and adjacent to the tip vortex prior to its interaction with the blade (BVI),
- determine the core size of the vortex,
- find the miss-distance between vortex and blade at their interaction. Necessary blade position measurements have been done by ONERA (TART),
- determine the circulation of the vortex.

The LDV-measurements have been carried out for five different rotor conditions:

1. Base-line case with 5.3° shaft angle,
2. Base-line case with 3.8° shaft angle,
3. Base-line case with 6.8° shaft angle,
4. HHC Low Noise (LN) case with 5.3° shaft angle,
5. HHC Low Vibration (LV) case with 5.3° shaft angle.

The present paper concentrates on case 1: Base-line case, α_{shaft} = 5.3° and gives some flow results also for case 5: HHC Low Vibration, α_{shaft} = 5.3°. The final experimental data obtained from the LDV-measurements are assumed as realistic inputs into numerical calculation procedures.

*Research Scientist, Institute of Fluid Mechanics.

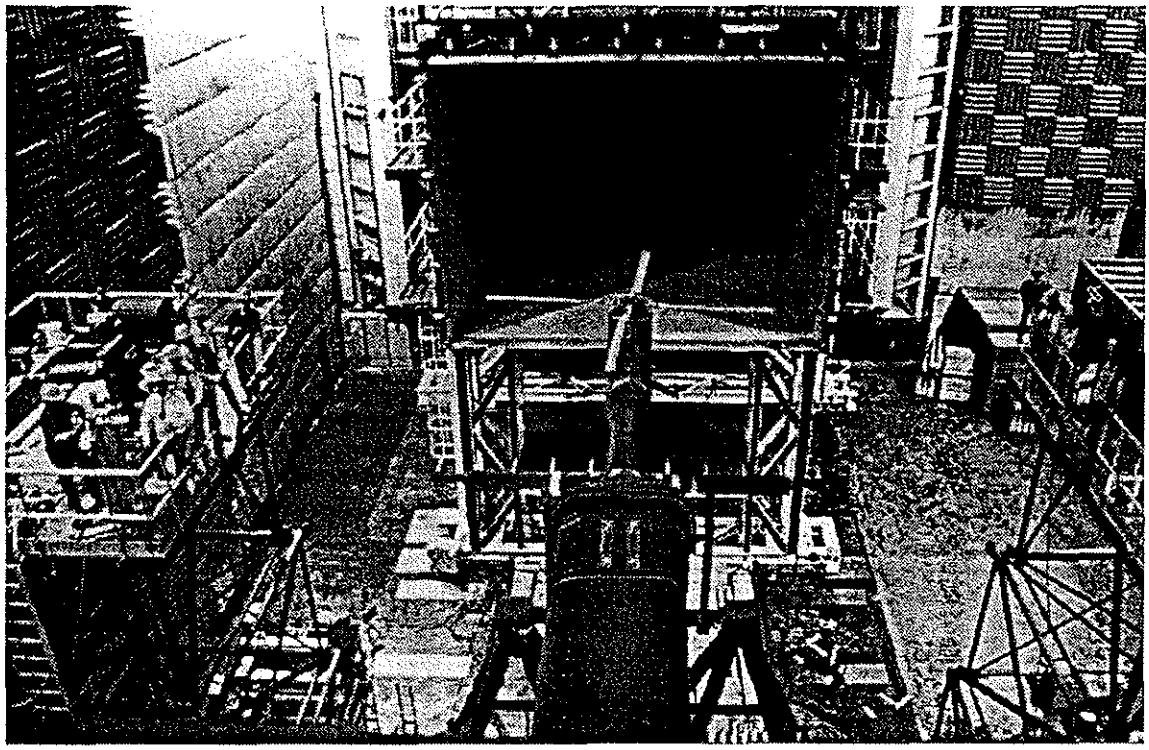

Fig.1: HART test set-up in the DNW open test section.
LDV-towers: left ONERA, right DLR.

In recent years the BVI-problem has been investigated in the Max Planck Institut für Strömungsforschung and at DLR Göttingen both experimentally [6] and numerically [7] as a two-dimensional model problem. In both cases the details of the interacting vortices have been estimated. It could not be confirmed that the flow phenomena occuring in the model flows are also exsistent on real rotors. With the LDV-data it is assumed to get more realistic input data and to start calculations with the "correct" initial conditions.

The 2D-time accurate Euler code described in [7] is proved to be a suitable tool to

- investigate in detail the time-dependent flow during the passage of the vortex
- determine the noise development and its radiation into the farfield

The latter problem has been solved by means of a Kirchhoff solution procedure. Allthough the flow calculations during BVI are limited to two dimensions, new considerable insight into the flow prior and during interaction between airfoil and vortex have been achieved. Sound pressure time histories as well as sound directivities can directly be compared with corresponding data measured by the microphone array during the HART-test campaign.

2. LDV-Measurements.

2.1 Measuring arrangement in DNW.

Fig.1 shows the BO-105 model rotor and the 3D-LDV set-up in the open test section of the DNW. The LDV-measuring plane was 10.75m above the tunnel floor. Transmitting and receiving optics of the LDV-system were installed on top of a special tower with a corresponding platform aligned with the rotor plane.

The DLR measurements took place on the advancing side of the rotor disc at ψ = 55° azimuth angle and at r/R = 0.75 radial position. From Laser Light Sheet (LLS) investigations accomplished by DNW [8] as well as from numerical calculations the location of the vortex with the most extensive effect with respect to BVI-noise generation was known in advance and the LDV-probe volume has been adjusted to this vortex position.

From the settling chamber of the windtunnel a small tube of seeding particles has been injected into the flow using dispersed oil particles with an average diameter below 1μm. The seeding injection set-up could be remotely controlled from the test stand to find an optimum position of the seeding probe.

2.2 Set-up of DLR 3D-LDV.

Fig.2 displays the set-up of the DLR 3D-LDV utilizing a 6 Watt argon ion laser. The light of the different wavelength was fed by mono-mode glass fiber to six individual transmitting optics which focus the laser light to the common measuring volume in the necessary measuring distance of 5m. The dimensions of the measuring volume are 0.25mm in diameter and 1mm in length.

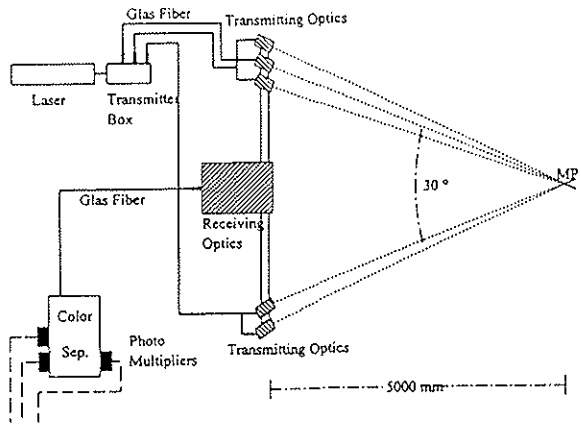

Fig.2: DLR 3D LDV set-up

A 500mm in diameter receiving optics included in the mechanical construction between the optical axis of the transmitting optics, collected the back scattered light from the seeding particles. Further details of the LDV-system and data reduction procedures are given in [9].

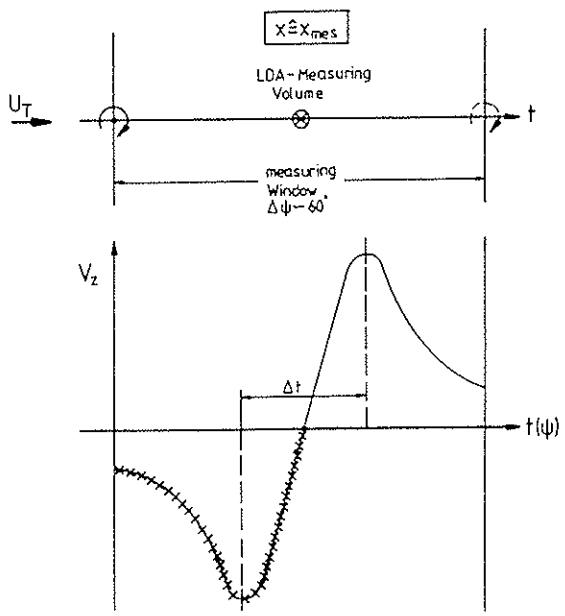

Fig.3a: LDV Measuring Procedure: Time-History.

2.3 LDV-Measurement Procedures.

For the measurement of velocity vectors by LDV two different procedures have been envisaged:

1. Time-history measurement
2. Velocity mapping.

In the first case the probe volume is fixed to one spatial position (see *Fig.3a*). Then the measuring window is opened ($\Delta\psi \approx 45°$) while the vortex is passing the probe volume. The corresponding velocity distribution (vertical component) as function of ψ (or time t) is sketched in Fig.3a. To cover the whole flow field adjacent to the vortex, the probe is then successively moved in vertical (z-) direction. The measuring time for each z-position is about 1min. For the total of 60 z-positions approximately 1hour of measuring time is necessary.

To find the core size from this procedure it has to be assumed that

- the convection speed of the vortex can be estimated
- the convection speed is constant within the measuring window.

The estimation of the convection speed with components in both axial and vertical directions is not straightforward. These values have been obtained by an iteration procedure described in section 2.4.1.

To determine the vortex core size independent from the convection speed, the velocity mapping procedure can be used instead.

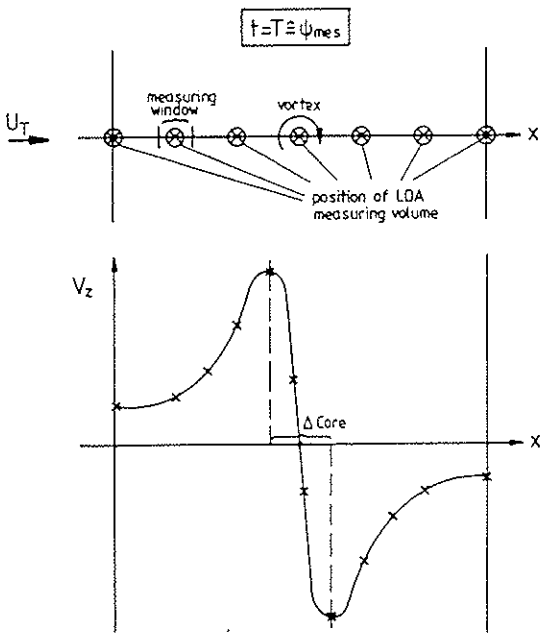

Fig.3b: LDV Measuring Procedure: Velocity Mapping.

Fig.3b shows the principle: Now the probe volume of the LDV is not only moved in vertical but also in axial direction. For each position a small axial measuring window is opened. With reference to a fixed trigger signal of the rotor, quasi steady velocity data of the periodic flow field are obtained. Thus the vortex position is kept fixed with respect to the measuring domain. With this procedure the core size of the vortex can directly be determined. But now a matrix of measuring points has to be covered by the LDV-probe volume leading to excessive measuring times (approximately one measuring day per case).

To save expensive windtunnel time, the first procedure was preferred. Additional effort was put into the post-processing of the LDV-data to solve the problem of determining the correct speed of the vortex (see section 2.4.1).

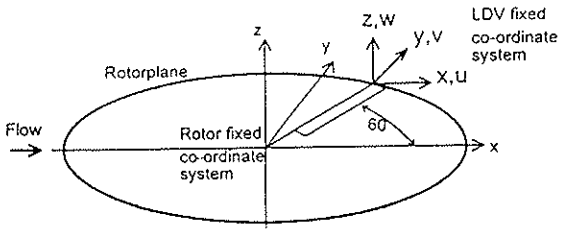

Fig.4: Coordinate System

2.4 Experimental Results.

The LDV-data displayed in the following sequences of figures have been measured in a LDV-fixed coordinate system (***Fig.4***) and were transformed into a rotor fixed system with its origin in the rotor-hub. ***Fig.5*** shows the measured velocity vector field in a x-z-plane where already estimated convection speeds of the vortex have been taken into account: $U_c = 33m/s$ ($\hat{=}$ tunnelspeed), $W_c = -10m/s$ (downwash). A vortical flow is clearly visible. In the lower part of the figure a band of increased velocities indicates the location of the wake of a preceding blade (starting at the right margin of the figure). In the following subsections the characteristic features of the vortex will be determined.

2.4.1 Vortex Convection Speed.

The velocity field in Fig.5 has been obtained with a rough estimate of the vortex convection speed. ***Fig.6*** displays the same flow region, but now areas of equal vorticity, defined by

$$rot(u) = \frac{1}{A} \cdot \oint \vec{u} \cdot d\vec{s}$$

with

$$\Gamma = \oint \vec{u} \cdot d\vec{s}$$

as the circulation around an area A with the path vector $\vec{s}$ ($\vec{u} \hat{=}$ local velocity vector) are shown.

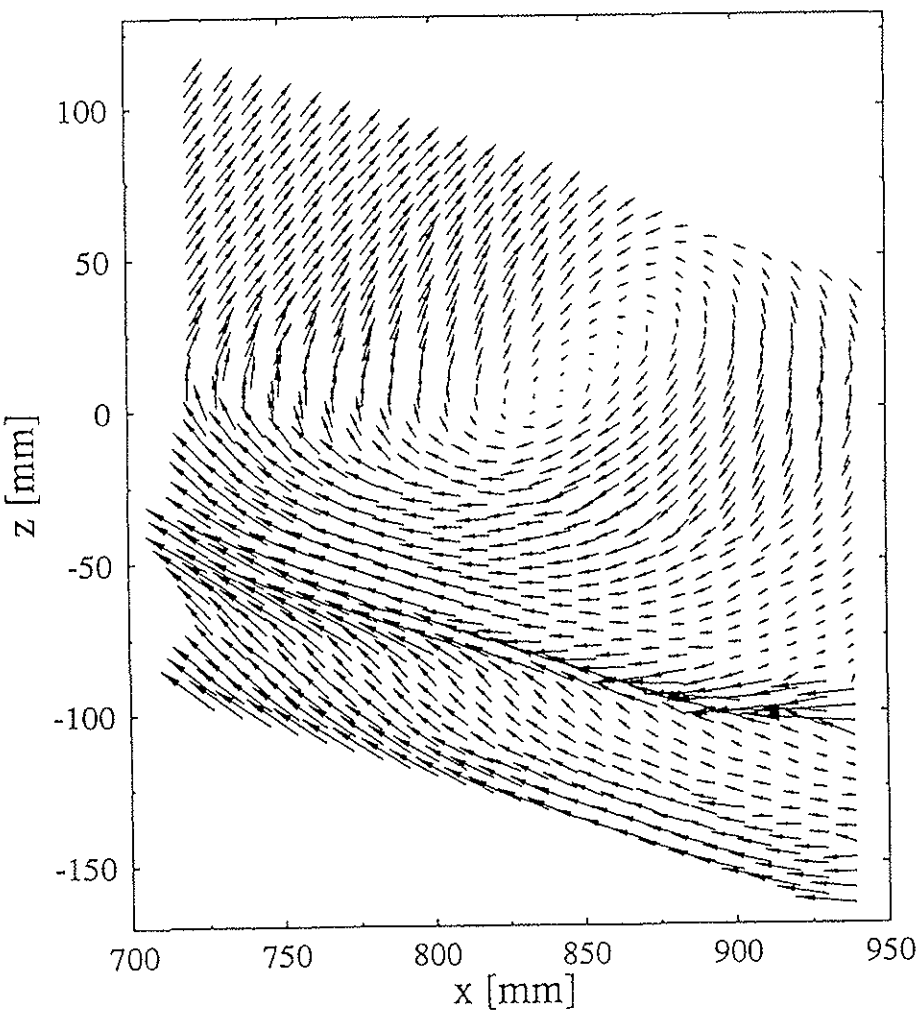

Fig.5: Measured Velocity Vector Field for Base-line Case, $\alpha_{shaft} = 5.3°$
Estimated Convection Speed: $U_c = 33m/s$, $W_c = -10m/s$

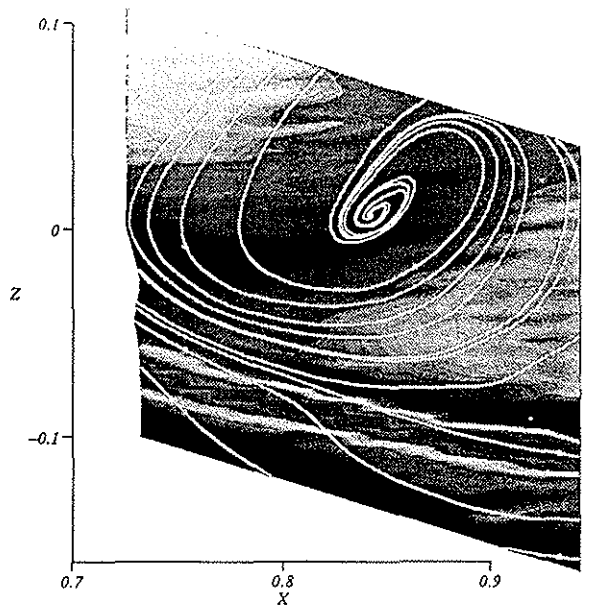

Fig.6: Vorticity Distribution and Selected Streamlines. Convection Speed as in Fig.5.

Except a vorticity increase along the wake the domain of the vortex shows only a rather small extension of vorticity, which is not appropriate in this case to determine the vortex center. In addition a selection of streamlines (the dots indicate the origin of these lines) have been calculated from the velocity field. The vortical structure of the flow is obvious. The streamlines are originating from a focal point. From vortex kinematics it is known that this type of flow structure occurs for a moving vortex, i.e. the convection speed estimated before does not correspond to the real vortex speed.

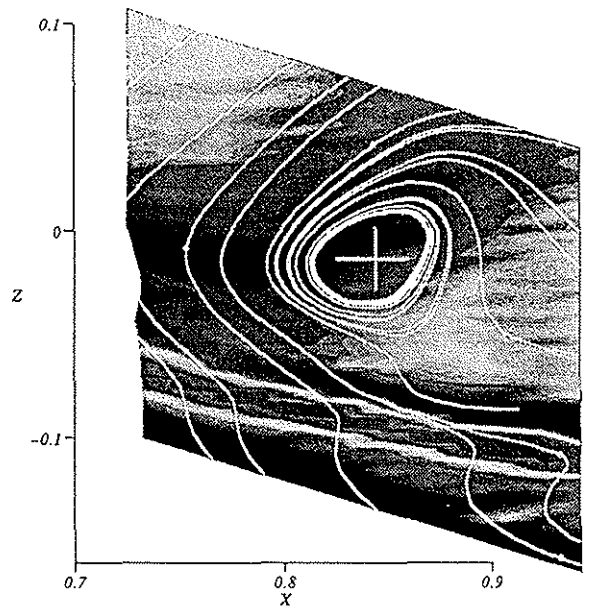

Fig.7: Vorticity Distribution and Selected Streamlines. Convection Speed: $U_c = 31 m/s$, $W_c = -10.5 m/s$.

Using the postprocessing tool COMADI [10] in a successive manner by modifying step by step the components of convection speed, the picture displayed in *Fig.7* is finally obtained. Now the components are:

$U_c = 31 m/s$, $W_c = -10.5 m/s$. The vorticity is of course not affected by this modification. However the streamlines show a rather different behavior: now a limiting streamline exists around a center. No streamlines can reach the vortex center. But the center can easily be determined from this plot. Compared to Fig.6 it has slightly been shifted.

Due to this distinguished behavior of streamlines and due to the fact that the center corresponds to the location of a (flat) vorticity maximum the corrected convection speeds of the vortex and its new position were taken for further investigations.

2.4.2 Vortex Core Size.

Figs.8 and 9 show velocity profiles along cuts through the vortex center of Fig.7. Fig.8 includes the profile in x-direction, Fig.9 gives the corresponding profile in z-direction. In Fig.8 the maximum and minimum velocity peaks due to the vortex can easily be detected. A dimensionless core size x/c=1.07 (c=0.121m, blade chord) is found as the distance between the two velocity peaks. The cut in the z-direction (Fig.9) shows in addition to the vortex effect also the influence of the wake of the preceding blade as has been discussed before. Due to this interaction between vortex and wake effects the core size can not easily be determined in this cut. A value for the core size of z/c=0.70 has approximately been found in this case.

The cut along x (z=constant), Fig.8, has to be corrected: The interaction between blade and vortex takes place at approximately $\Psi = 60°$ azimuth. The LDV-measuring area (x-z-plane) is located at $\Psi = 55°$. If it is assumed that the vortex generator is already parallel to the blade leading edge at this position, the cut along x has an angle of 35° with respect to the vortex generator: The core size for this cut is virtually larger and the corrected value is therefore: $x/c \cdot \cos 35° = 0.88$.

2.4.3 Vortex Miss-distance.

A rather complicated but straightforward step by step procedure has been applied to determine the miss-distance between vortex and interacting blade. For the present case 1 the interaction is assumed to occure at $\Psi = 60°$ azimuth angle. The following steps were done:

1. Determine the vortex center from the streamline plots with corrected speeds of the vortex (Fig.7).
2. Express the coordinates of the vortex center in the rotor-hub fixed coordinate system (Fig.4).
3. Take the measured position of the blade tip (at $\Psi = 60°$) close to the LDV-measuring plane ($\Psi = 55°$). The blade position was measured by ONERA using the TART-method (Target Attitude in Real Time).

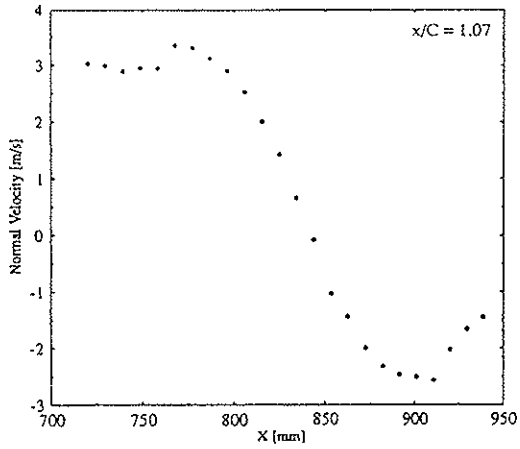

Fig.8: Velocity Profile Through Vortex Center in x-direction of Fig.7.

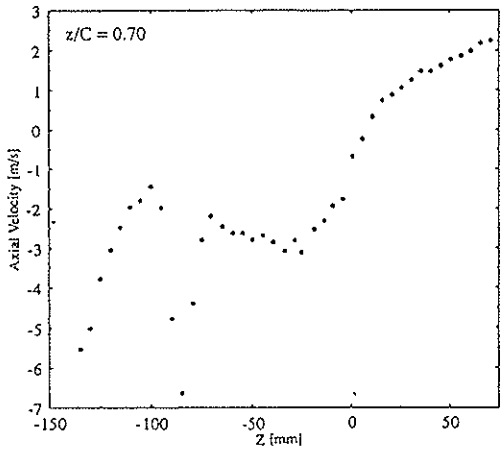

Fig.9: Velocity Profile Through Vortex Center in z-direction of Fig.7.

4. Interpolate the position of the vortex center at the LDV-measuring position (Ψ = 55°) to the interaction position (Ψ = 60°) with the assumption of an unchanged downwash velocity (W_c = $-10.5m/s$).
5. Determine the location of the blade section at r/R = 0.75 from the measured location of the blade tip by assuming a linear deflection of the blade from tip to root.
6. In the final step the vertical difference between the interpolated vortex center position and the location of the r/R = 0.75 blade section is calculated as the miss-distance between blade and vortex.

From this lengthy procedure a final value of z/c = -0.042 has been determined as miss-distance for the present base-line case: α_{shaft} = 5.3°. Corresponding numerical investigations of ONERA using free wake calculations yield a value of x/c = 0 for this case. Due to several uncertainties in both experimental and numerical procedures the correspondance between calculation and measurement is quite good. This holds also for most of the other cases of the HART-test campaign. (see [5]).

2.4.4 Vortex Strength.

Taking into account the vortex center (Fig.7) the circulation distribution can be derived by integrating the velocity distribution along boxes surrounding the center. The circulation is increased approximately linear with increasing distance from the vortex center. It reaches a maximum at about 50% of chord with a maximum value of Γ = $1.1m^2/s$.

2.5 Results of the HHC-Low Vibration Case.

Fig.10 shows the velocity vector field as measured by LDV and corrected with U_c = $33m/s$, W_c = $-10m/s$ convection speed of the vortex for the Higher Harmonic Control Low Vibration case with α_{shaft} = 5.3°.

In this case some surprising flow structures can be detected including a double vortex system with a larger but less intensive vortex and a smaller but stronger vortex nearly above the first one. The lower vortex is rotating in clockwise direction, i.e. in the same sense as the single vortex of Fig.5 (Base-line case). The upper and stronger vortex however rotates in anti-clockwise sense. Applying the same procedure as in the base-line case a corrected convection speed of U_c = $31.5m/s$, W_c = $-8.5m/s$ is obtained (see Fig.11). With these components the streamlines around the lower vortex have a limiting value. For the upper vortex the streamlines show still a spiral structure.

Several conclusions can be drawn from these observations:

- the existence of two counterrotating vortices indicates a change of sign of the blade loading at the tip region where the vortices originate. The counterclockwise rotating tip vortex develops due to a negative gradient of bound circulation at its origin.
- the vortex system is conserved downstream as separated vortices with slightly different convection speeds. Possibly the centers of the two vortices move around a common center.

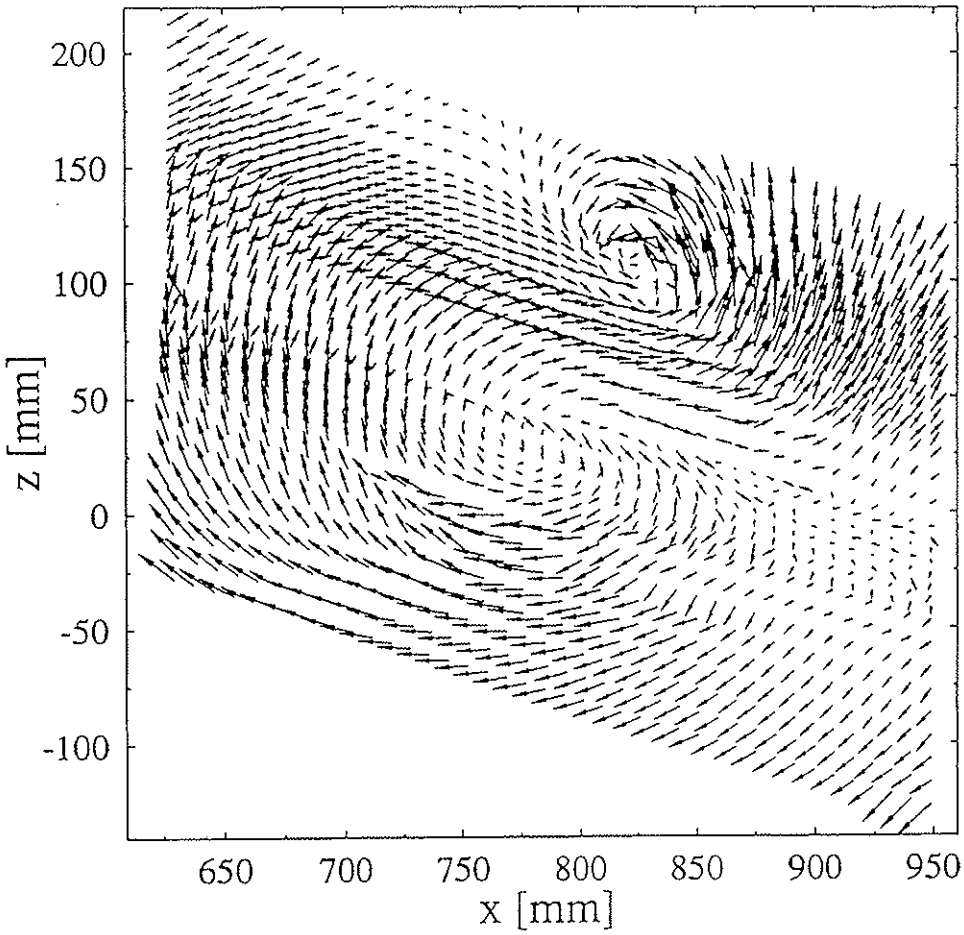

Fig.10: Measured Velocity Vector Field for HHC Low Vibration Case: α_{shaft} = 5.3°.
Estimated Convection Speed: U_c = 33*m/s* , W_c = –10*m/s*.

- the vorticity distribution (Fig.11) shows a distinct minimum of vorticity (counter clockwise) for the upper vortex. The vorticity content of the lower (clockwise rotating) vortex is comparable to the base-line cases.

From these experimental data it is shown for the first time how the specific HHC-settings for Low Vibration affects the blade loading at the origin of the vortex and creates a double vortex structure with the less intensive vortex close to the blade (miss-distance z/c = 0.196) and the stronger vortex far above the blade (miss-distance z/c = 1.21). It is obvious that this system develops considerable BVI-noise (as has been measured) similar as in the base-line cases.

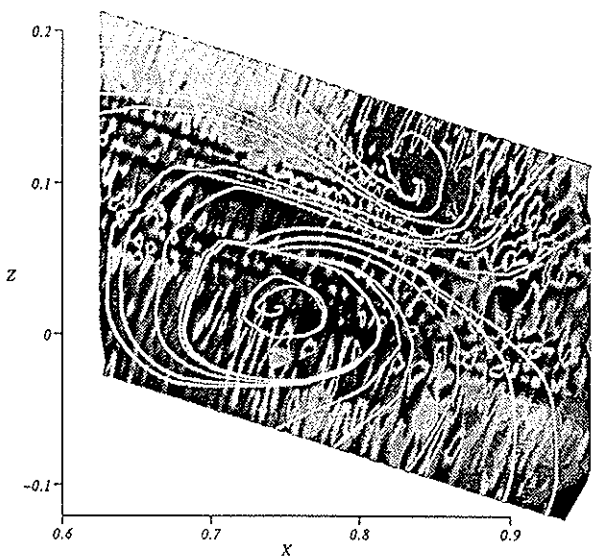

Fig.11: HHC Low Vibration Case: α_{shaft} = 5.3°.
Vorticity Distributions, Selected Streamlines.
Convection Speed: U_c = 31.5*m/s* , W_c = –8.5*m/s*.

3. BVI-Calculations with Time-accurate Euler Code.

3.1 Numerical Code.

For the numerical investigation of Blade-Vortex Interaction a finite volume scheme has been used to solve the 2D-unsteady Euler equations, [7]. The scheme works on unstructured grids which consist of triangles. The numerical flux is calculated with the flux-difference splitting method using Osher's approximate Riemann solver. To improve the accuracy of the solution and to avoid excessive numerical dissipation, a higher order procedure is applied for spatial interpolation. Without this extra numerical effort the vortex as well as the generated sound waves would be damped in an unacceptable way.

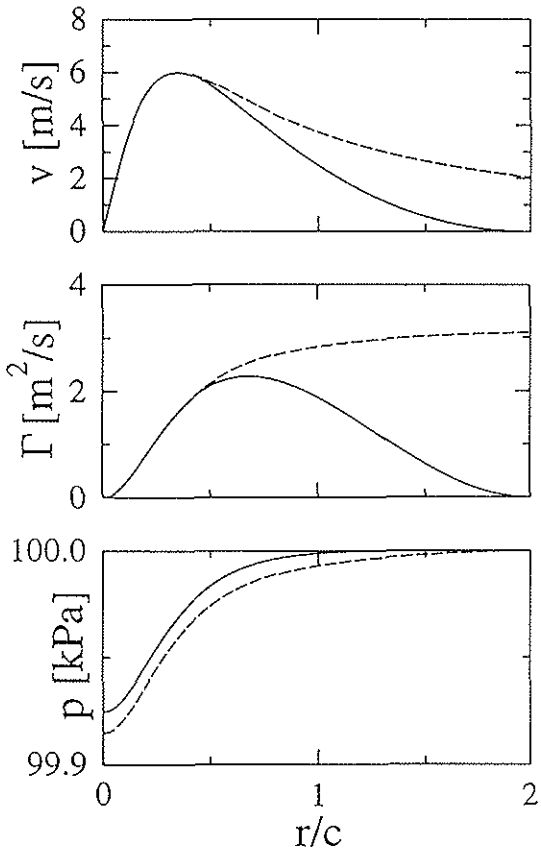

Fig.12: Distributions of: Tangential Velocity (top), Circulation (middle), Pressure (bottom).
Dashed Curves: Original Lamb-Vortex
Solid Curves: Modified Lamb-Vortex

The calculation starts with a steady flow around a profile where a vortex is inserted far upstream. At the beginning this vortex is convected downstream. When it reaches the airfoil the actual interaction takes place. Then the vortex (or the remainings of it) are convected further downstream. Meanwhile the generated sound waves are propagating into the whole computational domain. To minimize the influence of the boundary on the inner solution, higher-order nonreflecting boundary conditions are applied along the outer boundary. This procedure has the effect that sound waves which reach the outer boundary simply leave the computational domain as if the domain would continue to infinity.

Special emphasis has been placed on a realistic modelling of the incoming vortex. Desirable would be to know the complete field data of velocity, density and pressure inside the real vortex. But due to experimental restrictions informations are obtained only at a limited number of points. Thus the experimental data give only a rough idea of the vortex strength and extension. To determine the exact structure of a compressible vortex, a model has to be used. In the present case several assumptions are necessary:

- The vortex has to fulfill the radial momentum equation, i.e. the vortex is really a steady solution of the Euler equations. Otherwise the vortex itself would be unsteady and generate disturbances already without any interaction.
- The radial distribution of the tangential velocity and the entropy are prescribed.

The whole procedure to compute and insert the vortex into the flow field is described in detail in [7]. The velocity distribution which is used for the present calculations is based on the vortex model of Lamb. For the entropy simply a constant value is assumed.

In Fig.12 the radial distributions of various quantities of the model vortex are shown. Two variants of the model vortex are plotted: The solid lines correspond to the one actually used in the calculations. The dashed lines are for a model vortex using the original Lamb formula for the velocity. In the latter case the model vortex has an infinite extension. The velocity increases from zero in the vortex center to its maximum which is at r/c=0.35 in the given example. This point is defined as the core radius. For larger values of r the velocity decreases and tends to zero as r goes to infinity.

To avoid difficulties with the initial conditions at boundaries the Lamb formula was modified to give a vortex with finite extension (solid curves in Fig.12). Inside the core the variants are almost identical. But outside the core the velocity decreases steaper compared to the infinite vortex and reaches zero at the prescribed radius of r/c=2.0 (referred to airfoil chord). These differences cause also deviations in the distributions of the other quantities as can be seen in Fig.12.

For the finite vortex the circulation has a maximum at a certain radius, which is larger than the core radius, and the circulation vanishes smoothly when r/c reaches 2.0. In the original Lamb model the circulation grows monotonously with r and reaches its maximum at infinity. But the measurements have shown that the real vortex has indeed a distinct maximum circulation at a certain radius. It seems that the finite vortex model, which has definitely numerical advantages, does also reasonably model the real situation.

3.2 Calculation of BVI-Flow Fields Using LDV-data as Input.

With the different quantities measured by LDV and discussed in the previous sections the characteristics of the vortex can now be specified for the numerical calculations. The following quantities have to be taken as input into the vortex model:

- height of the velocity peak, corresponding to vortex strength
- location of the velocity peak, indicating the vortex core size
- extension of circulation into the farfield
- sense of rotation of vortex
- Mach number of vortex and undisturbed flow with respect to airfoil
- airfoil shape and its incidence
- vertical distance between vortex and airfoil at interaction (miss-distance)

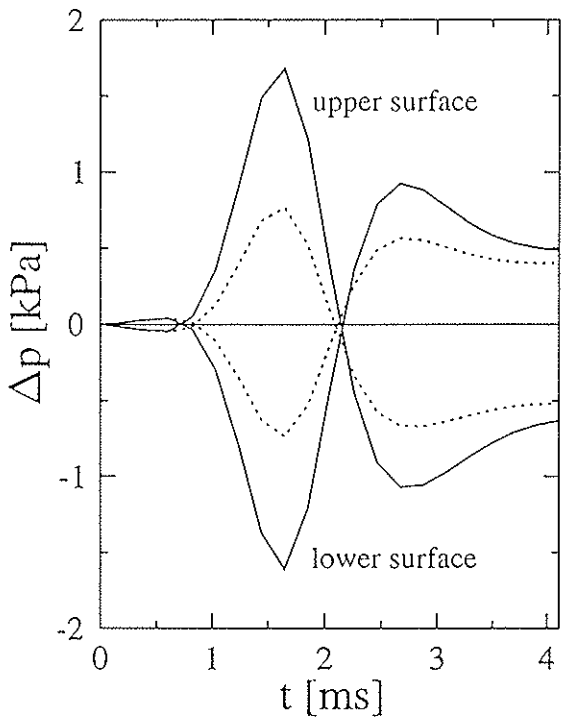

Fig.13: Pressure Fluctuations due to Vortex Passage at 3% airfoil upper/lower surface.
Dashed Curves: $\pm 3m/s$-peak velocity
Solid Curves: $\pm 6m/s$-peak velocity

For the base-line case 1 with $\alpha_{shaft} = 5.3°$ the following quantities have been obtained before and can be listed as follows:

maximum velocity	$\pm 3m/s$
vortex core size	0.7c
extension of circulation	r/c=2
rotation direction	clockwise
Mach number	0.57 (at r/R=0.75)
airfoil	NACA23012
miss-distance	-0.042c (below airfoil)

With these parameters the numerical calculations have been carried out and as a first check the pressure fluctuations at the blade due to the effect of the vortex are investigated and compared with measured pressures, [1]. Fig.13 shows the pressure fluctuations (mean values subtracted) at 3% lower/upper airfoil surface as function of time. The dotted curves show results for the $\pm 3m/s$-maximum velocity case. A Δp of 1.5kPa has been calculated. The corresponding experimental data (Polar/Dpt:99/1333 in [1]) however show a Δp of approximately 3kPa for this BVI-case (see height of the BVI-spikes in figure, page 253 of [1]).

This coincidence between the $\pm 6m/s$-maximum velocity case and the corresponding calculated and measured pressure response at the airfoil indicates that a stronger vortex has to be used in the calculations to generate the measured pressure fluctuation.

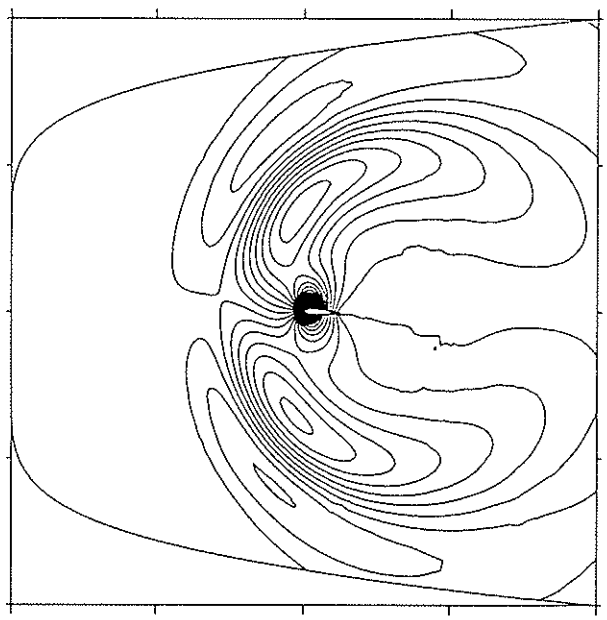

Fig.14: Instantaneous Pressure Contours (Steady Pressures Subtracted) During Vortex Passage.

The discrepancy may be caused by several reasons:

- numerical errors
- unexact vortex model
- uncertainties in the ensemble averaging procedure of LDV

The latter effect has been investigated by a simple model calculation, [11], which shows the tendency to measure a too small peak velocity inside the vortex.

In the following numerical investigations the $\pm 6 m/s$-velocity case has been taken. All other parameters were kept unchanged. Fig.14 shows instantaneous pressure contours at the time instant when the vortex has passed the airfoil. Only pressure differences (steady pressure field subtracted) are indicated. At this time the remainings of the vortex are located approximately three chord lengths downstream of the airfoil. Pressure waves have already been formed almost symmetrically propagating towards the farfield. The exact sound wave directivity will be determined in the following section.

3.3 Kirchhoff Solution Procedure for Calculation of Noise Radiation.

For the analysis of the farfield sound generated by the parallel blade vortex interaction the pressure fluctuations at certain points in the far field have to be computed.

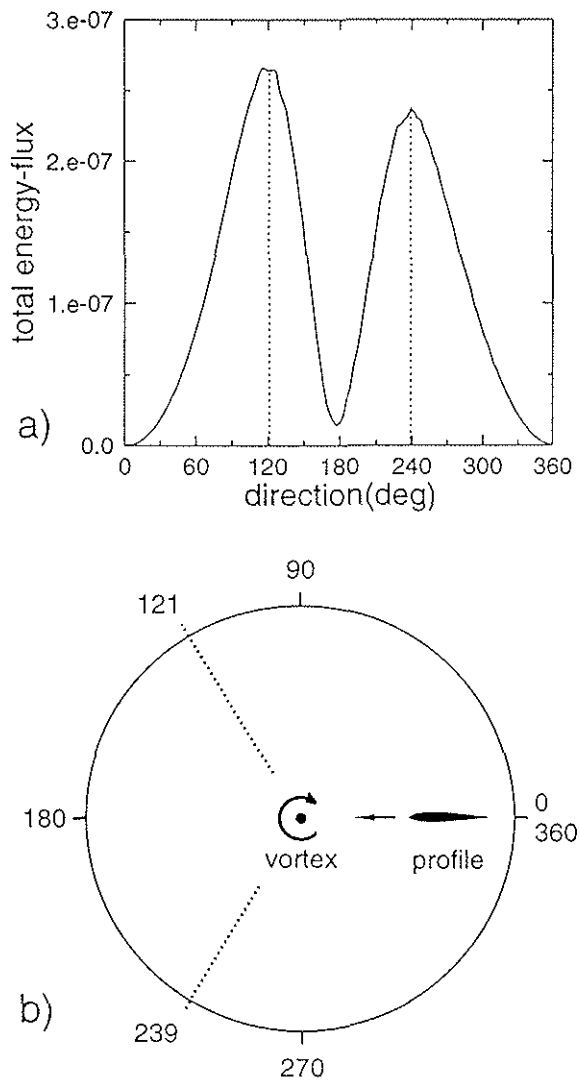

Fig.15:
a) Directivity Distribution of Total Energy Flux Generated by Emitted Sound Waves.
b) Geometry in Reference Frame Fixed to Free Stream Velocity.

From an acoustic point of view the computational domain used for the Euler calculation represents only the midfield of the generated sound. An extension of the computational domain to calculate the pressure also at farfield points directly by the Euler code would cause an unrealistic high amount of numerical effort. For the computation of weak acoustic waves an acoustic formulation is more suitable than a nonlinear code. Therefore Kirchhoff's method is used to compute pressure fluctuations at farfield points.

A similar approach was used in [12] to calculate BVI-noise. The main difference between the present procedure and reference [12] is the application of an Euler code instead of a small perturbation theory.

A close surface, the so called Kirchhoff surface, is defined in the flow field. This surface should cover all regions where nonlinearities are important and where all sound sources are included. It is assumed that outside of this surface the acoustic equations describe the propagation of sound waves exactly. In our two-dimensional case the Kirchhoff surface is a one-dimensional curve which was chosen to be a circle with radius of three times the chord. The center of the circle is the c/2-point of the airfoil. For the actual Kirchhoff computations this circle is discretized by 400 points.

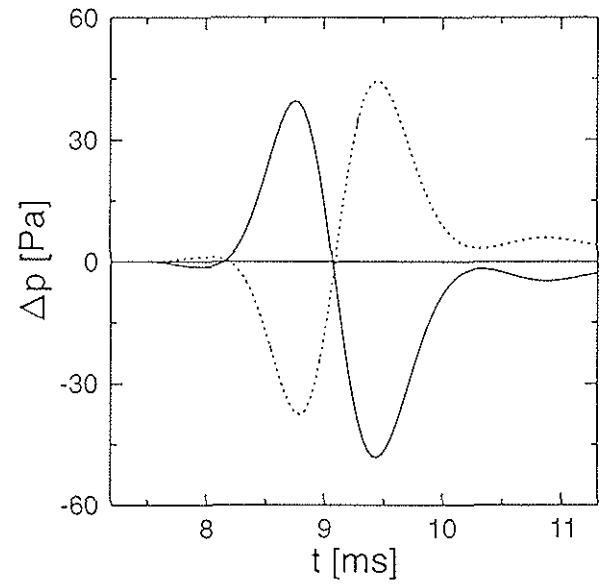

Fig.16: Pressure Time History in Two Farfield Points at Total Energy Maximum.
Solid Curve: 121°
Dashed Curve: 239°

At these points the pressure and its spatial derivatives are interpolated and stored at each time step of the Euler calculation. With these data as input the pressure at each point outside the Kirchhoff surface can be calculated by the Kirchhoff method. Numerical experiments have shown that this method is critical with respect to unexact interpolations of the spatial pressure derivatives. To achieve more accurate results the grid

used in the Euler computations is refined specifically in the region adjacent to the Kirchhoff surface.

To analyse the directivity of the generated sound in the farfield, a reference frame fixed to the free flow is considered. In this reference frame the vortex is at rest and the airfoil is passing it with the prescribed Mach number. A small movement of the vortex from its initial position is only caused by the disturbance of the airfoil. Around the initial position a circle with radius R=20c is constructed. The pressure time history and the radial derivative of the pressure is computed at 128 points along this circle. With these values the energy is calculated, which is transported at each instant of time by the acoustic waves into the radial outward direction of the circle. This energy flux is integrated in time over an intervall covering all waves generated during the interaction. This total energy flux is plotted in Fig.15a as a function of circular angle where zero degree is defined opposite to the direction into which the airfoil is moving. 90° is normal to this direction above the path of the airfoil. 180° is in moving direction and 270° below the path respectively. Fig.15b shows the geometric details.

The curve in Fig.15a displays two distinct maxima of total energy flux. The first one is located at 121° and the second one at 239°. Both directions are indicated in Fig.15b. As an example the pressure time histories at the two points on the circle which correspond to the maximum energy fluxes are plotted in Fig.16. The amplitudes referring to the point above the airfoil path (solid curve) are slightly larger compared to their downward directed counterpart: More energy is scattered into the direction above the airfoil path. Of more practical concern however is the energy scattered into the region below the path,i.e. noticed by an observer at the ground. A strong directivity of emitted sound is predicted already from the present 2D-calculations. It is pointed out in the next section that these observations fit surprisingly good to corresponding experimental data measured by microphones in the farfield of the model rotor.

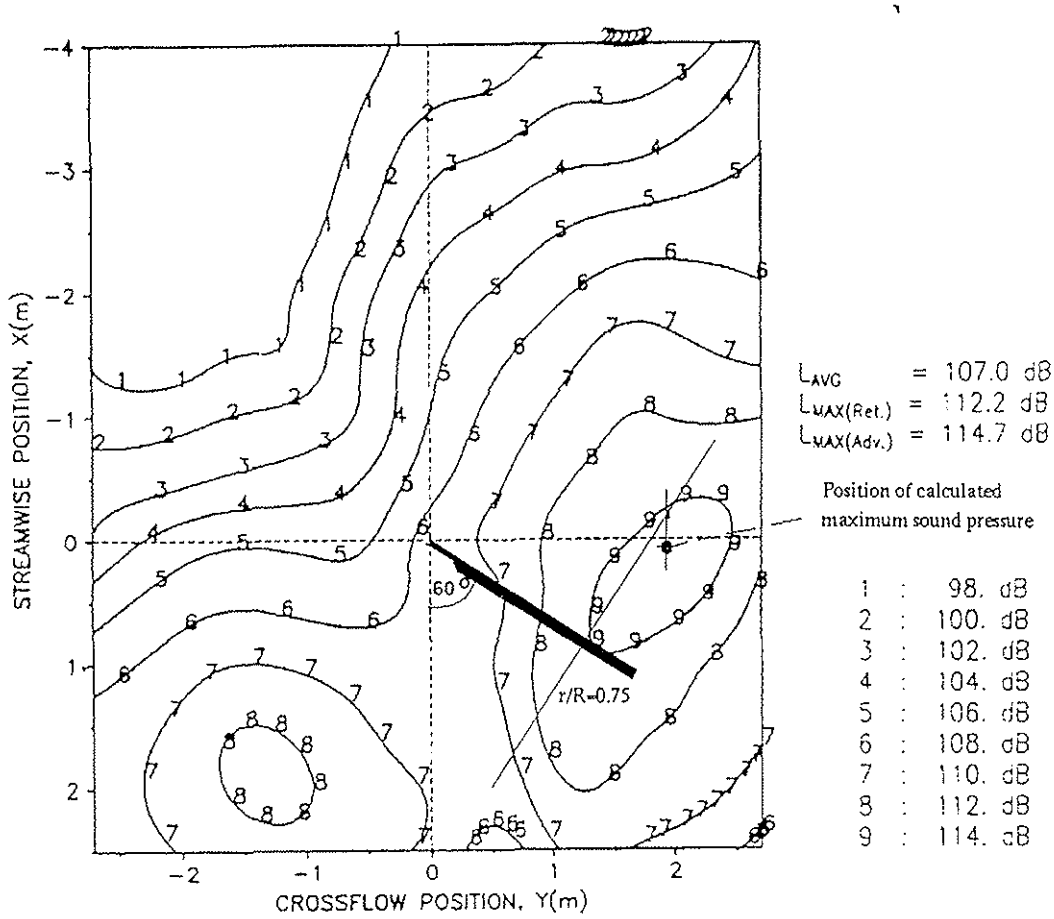

Fig.17: Sound Pressure Contours Measured by Microphone Array during Helinoise-Test (2.3m below Rotor Disc). Location of Calculated Maximum Sound Pressure Level.

3.4 Comparison of Calculated Noise Data with Measured Microphone Data.

The calculated sound pressure time histories plotted in figure 16 are comparable with the measured values by microphones. At microphone Nr.10 (maximum BVI-noise of Polar/Dpt:99/1333 in [1]) the sound pressure amplitude reaches a value of $\Delta p = 80Pa$ compared to $\Delta p = 86Pa$ from the calculations (Fig.16). The structure of the signal: a minimum follows a maximum (dashed curve in Fig.16, downward direction) is the same for both measured and calculated signals. Fig.17 shows sound pressure contours measured by a microphone array at 2.3m distance below the rotor disc. Taking into account the direction of the maximum total energy flux (at 239°*downwards*) the dot in Fig.17 gives the corresponding position of the calculated sound pressure maximum. A linear correction has been applied taking into account the wintunnel speed.

4. Conclusions, Future Activities.

3D-LDV flowfield measurements have been carried out in tip vortices prior to blade vortex interaction (BVI) during the HART-test campaign. Details of the vortices like core-size, strength, circulation and miss-distance could be determined from these measurements and are assumed as realistic inputs into numerical codes to calculate BVI-noise generation and radiation.

The different parameters from the LDV-measurements were taken as input into a 2D-time accurate Euler-code combined with a Kirchhoff solution procedure to calculate sound pressures in the farfield. It was found that the measured peak to peak velocities inside the vortex were too low to produce the measured pressure fluctuation during BVI. With an increase of the peak to peak velocities by approximately a factor of two, keeping all other parameters unchanged, the measured pressure fluctuation at the blade and the measured sound pressure signature and directivity in the farfield matched the calculated data sufficiently.

One reason for the discrepancy in vortex strength may be attributed to the ensemble averaging procedure of the LDV data. Small movements of the vortex, which have been observed from Laser-Light-Sheet (LLS) visualization during the test, may be the reason of smearing the velocity peaks.

For future tests it is therefore envisaged to apply a different measuring technique, the particle image velocimetry (PIV). With this method a 2D- *instantaneous* flow field can be measured and the problems occuring with the ensemble averaging procedure are avoided. Efforts are further done in DLR to extend the PIV-technique to three dimensions.

5. References.

1. Splettstösser,W.R. Junker,B. Schultz, K.-J., Wagner,W., Weitemeyer,B., Protopsalkis,A., Fertis,D.
   The Helinoise Aeroacoustic Rotor Test in the DNW.
   -Test Documentation and Representative Results-
   DLR-Mitt. 93-09 (1993)
2. Gelhar,B., Junker,B., Wagner,W.
   DLR-Roter Teststand Measures Unsteady Rotor Aerodyn. Data.
   Paper no.C8,Proceedings 19th European Rotorcraft Forum,Cernobbio,Italy, 1993.
3. Seelhorst,U., Sauerland,K.-H., Schmidt,F., Vollmers,H., Bütefisch,K.A., Geissler,W.
   3D-Laser-Doppler-Velocimeter Measurements within the HART-Test Program
   DLR IB 223 94A37 (1994).
4. Yu,Y.H. et al
   HHC Aeroacoustic Rotor Test at the DNW
   -The Joint German/French/US Project-
   20th European Rotorcraft Forum,Amsterdam,The Netherlands,1994.
5. Kube,R. et al
   Initial Results from the Higher Harmonic Control Aeroacoustic Rotor Test (HART) in the German-Dutch Windtunnel.
   75th AGARD Fluid Dynamic Panel Meeting on Aerodynamics and Aeroacoustics of Rotorcraft.
   Berlin,Germany,Oct.1994.
6. Obermeier,F., Schürmann,O.
   Experimental Investigation on 2D Blade-Vortex Interaction Noise.
   15th AIAA Aeroacoustic Conference, Long Beach,Ca,Paper no 93-4334, 1993.
7. Ehrenfried,K., Meier,G.E.A.
   Ein Finite Volumen Verfahren zur Berechnung von instationären transsonischen Strömungen mit Wirbeln.
   DLR-Forschungsbericht 94-33 (1994).
8. Mercker,E., Pengel,K.
   Flow Visualization of Helicopter Blade-Tip Vortices.
   Paper no 26,Proceedings 18th European Rotorcraft Forum,Avignon,Sept.1992.
9. Seelhorst,U., Bütefisch,K.A., Sauerland,K.-H.
   Three Component Laser Doppler Velocimeter Development for Large Windtunnel.
   ICIASF 93 Record,pp 33.1-33.7 (1993).
10. Vollmers,H.
    Diagnostic and Visualization Tools for Flow Fields.
    26th ISATA Symposium,
    13-17 Sept.1993,Aachen,
    Germany,pp 529-535.
11. Seelhorst,U.
    Private Communication,Aug.1995.
12. George,A.R. Lyrintzis,A.S.
    Acoustic of Transonic Blade-Vortex Interactions.
    AIAA J. Vol.26,No.7,July1988,pp769-776.